J Infrared Milli Terahz Waves
DOI 10.1007/s10762-015-0241-x

Broadband Sub-terahertz Camera Based on Photothermal Conversion and IR Thermography

M. Romano[1] · A. Chulkov[2] · A. Sommier[1] · D. Balageas[1] · V. Vavilov[2] · J. C. Batsale[1] · C. Pradere[1]

Received: 29 September 2015 / Accepted: 21 December 2015

Abstract This paper describes a fast sub-terahertz (THz) camera that is based on the use of a quantum infrared camera coupled with a photothermal converter, called a THz-to-Thermal Converter (TTC), thus allowing fast image acquisition. The performance of the experimental setup is presented and discussed, with an emphasis on the advantages of the proposed method for decreasing noise in raw data and increasing the image acquisition rate. A detectivity of 160 pW $Hz^{-0.5}$ per pixel has been achieved, and some examples of the practical implementation of sub-THz imaging are given.

Keywords Sub-terahertz imaging · Photothermal converter · Infrared thermography · Focal plane array · Non-destructive testing

1 Introduction

The far-infrared, or sub-terahertz (THz), region of the electromagnetic spectrum reveals specific interactions between radiation and matter and can be efficiently used for inspecting materials that are transparent in the THz wavelength band. THz technology is increasing in popularity as a new and powerful technique for imaging and tomographic analysis in many application fields [1–4].

Until now, optical radiometry using THz detectors has been scarcely studied; the majority of the published THz images were obtained using scanning systems with a single detector [5–7]. However, some traceable measurements of the absolute THz power have recently been performed [8, 9]. Currently, this technique based on scanning systems is being substituted with THz imaging units that implement staring sensor arrays [10–12].

✉ C. Pradere
c.pradere@i2m.u-bordeaux1.fr

[1] I2M TREFLE, UMR CNRS 5295, Esplanade des Arts et Métiers, 33405 Talence, France

[2] Tomsk Polytechnic University, Lenin Av., 30, 634050 Tomsk, Russia

Published online: 07 January 2016

Because several THz imaging technologies are in competition, an efficient method for determining the characteristics of THz detectors is required to develop a complete and powerful system that offers high-sensitivity, broadband analysis, and high frame rate acquisition [13]. In fact, the performance of THz detectors is assessed by considering either their noise limitations, represented by the noise-equivalent power (NEP) or their sensitivity [14]. Recently, a THz camera that includes an uncooled array (160 × 120 pixels) microbolometer with a nominal pitch of 52 μm was developed at Institut National d'Optique (INO; Québec, Canada). The reported results regarding the advances in obtaining transmission and reflection images are very promising [15]. Several works have reported the comparison [16] and development of high-sensitivity microbolometers [17], with a specific design for THz detection based on an innovative use of antennas and resonant cavities. The results demonstrate that improved sensitivity and the proper choice of acquisition frequency are essential for ensuring the imaging of low-power signals.

In some previous investigations, a method for measuring the absolute power value of far-infrared radiation was reported to propose a calibration methodology based on the Seebeck effect for the photo thermal converter [18]. Additionally, an experimental study using single or array thermal sensors for real-time room temperature far-infrared image acquisition was reported [19], and the sensitivity between the different techniques was evaluated using the obtained images. Such investigations include the use of an IR camera coupled with a photothermal converter, called a THz-to-thermal converter (TTC), which enables the efficient absorption of the incident multispectral sub-THz radiation and its conversion into IR radiation.

This work presents both the particular imaging instrumentation and the performance evaluation of this instrumentation. After describing the experimental setup, we discuss the efficiency of the quantum sensor in sub-THz imaging acquisition, as well as the processing method based on the so-called four-image processing algorithm. Subsequently, this work presents an analysis of the combination of instrumentation (photothermal converter and the cooled camera) and a discussion on the influence of several parameters, such as the thermal efficiency of the TTC (photothermal conversion rate), the incident source shape, and the power density of the light source, which enable the proposal of a broadband THz camera. Finally, the results regarding the acquisition of sub-THz images using the proposed camera are presented. This work demonstrates that a quantum infrared camera coupled with a TTC constitutes a robust and promising instrumentation in terms of frame rate and sensitivity. This instrumentation can be considered for further applications, such as real-time non-destructive monitoring techniques.

2 Technical Specifications of the Camera

2.1 Experimental Setup

Figure 1 presents a photograph of the experimental setup. The core of the system is a 200-mW Gunn diode of 110 GHz (wavelength of 2.8 mm) from Virginia Diodes, which is used as a THz source (Fig. 1 (1)). A mechanical shutter from Uniblitz is used to modulate the continuous beam radiation (Fig. 1 (2)). To obtain THz images of test objects, a THz lens designed by ALPhANOV is used with a magnification of 1 (Fig. 1 (3)). To convert the incident THz radiation into the IR domain, a lens from NeTHIS (where the TTC is integrated, Fig. 1 (4)) is coupled with a FLIR SC 7000 infrared (IR) camera (Fig. 1 (5)). The IR camera is equipped with a 256 × 320 pixel array of MCT (mercury cadmium telluride) detectors working in the spectral band of 7 to 14 μm (NETD of 20 mK). The sensitivity at room temperature is 80 pW/pixel for an integration time of 600 μs.

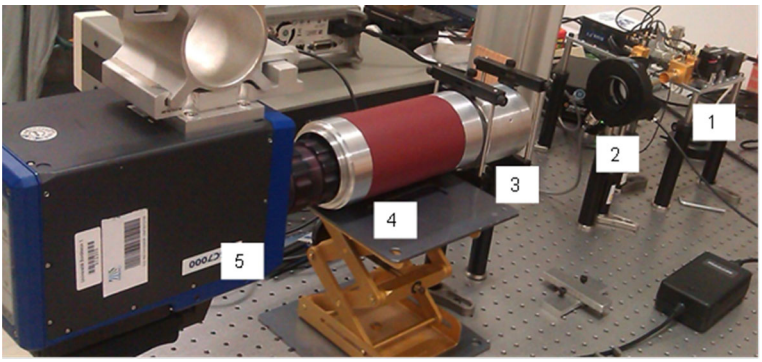

Fig. 1 Photograph of the experimental setup: *1*, Gunn diode of 110 GHz; *2*, mechanical shutter; *3*, THz objective of magnitude 1; *4*, THz-IR objective with photothermal converter; and *5*, IR camera

2.2 Terahertz-IR Photothermal Converter

The TTC is a very thin and homogeneous sheet of low resistance carbon-based paper (industrial Nethis patent [20]) with a diameter of 5 cm and a thickness of 15 μm (Fig. 2a, c). The thermal diffusivity of the converter was estimated to be 4.16×10^{-7} m^2 s^{-1} using classical thermal characterization techniques [18, 19]. Thermally, a converter can be considered to be a thin homogeneous medium subjected to convective/radiant heat losses and containing an internal heat source that models the incident THz radiation. Due to the small thickness and large lateral dimensions of the TTC, the temperature through the converter (i.e., in the z direction) can be assumed to be constant. Moreover, because the absorption of the incident THz radiation is a function of the thickness (the Beer-Lambert law), the heat source power can be assumed to be constant along the z direction because of the large ratio between the wavelength (approximately 3 mm) and the converter thickness (15 μm).

The efficiency of the thermal conversion, which is schematically shown in Fig. 2b, is based on the photothermal principle and depends on the following: (i) the optical properties in the millimeter and far-infrared bands, (ii) the thermal properties of the converter, (iii) the heat loss coefficients, (iv) the integration time of the IR camera, and (v) the incident radiation profile.

Note that because of its optical properties, a thin carbon film can be regarded as a blackbody (Fig. 3a) with an emissivity close to 1 in the 7 to 14 μm wavelength

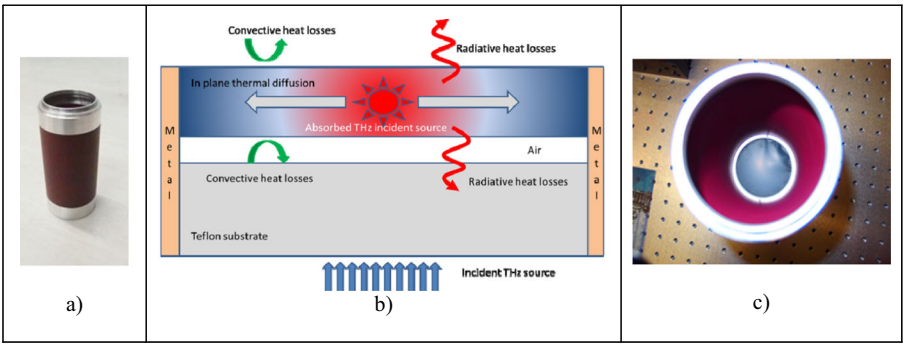

Fig. 2 The TTC: **a** global view, **b** schematic layout and physical phenomena involved in the conversion, and **c** magnified view from the top, showing the photothermal film

range and as a semi-absorbing medium in the millimeter wavelength band (Fig. 3b).

2.3 Acquisition Rate

Performing measurements using such millimeter-wave cameras (Fig. 4) requires the use of a proper THz integration time (IT). In fact, the FLIR SC 7000 IR camera is used in the snapshot mode, in which both the IT and the acquisition rate can be respectively controlled in the range from 1 μs to 1 ms for the IR-IT and from 1 Hz to 1 kHz for the acquisition frequency range (top of Fig. 4). The idea is to synchronize a modulated THz signal generated by a pulsed or modulated THz beam with the acquisition signal of the IR camera.

In this way, a different THz frequency is produced in the range of 0.1 to 1000 Hz, and the thermal response of the photothermal converter is recorded as the increasing slope of the THz excitation signal (bottom of Fig. 4). Finally, by using a proper data processing algorithm (see Sect. 4.2), a single resulting image at the THz modulation frequency is extracted. As shown in the modeling section, the THz-IT should never be higher than the thermal diffusion characteristic time (approximately 1 s in general), which is determined by the thermal properties of the photothermal converter and the pixel format of the IR image.

Other studies have been reported regarding the acquisition rate, providing fruitful discussions on the advantages and disadvantages of this technique [3, 7].

2.4 Signal Processing

A lock-in technique based on the four-image analysis approach [21] was used to measure the THz response:

$$A(x,y) = \frac{\sum_{i=1}^{\mathrm{Np=Nppp}/4} \sqrt{[T(x,y,i+2\mathrm{Np}) - T(x,y,i)]^2 + \left[T(x,y,i+\mathrm{Np}) - T\left((x,y,i+3\mathrm{Np})\right]^2}}{2\mathrm{Np}}, \quad (1)$$

where $A(x,y)$ defines the THz spatial amplitude response over the sample surface, T is the temperature signal measured by the IR camera, Nppp is the number of points per period, Np is the number of points within a quarter of a period, and x and y are spatial coordinates.

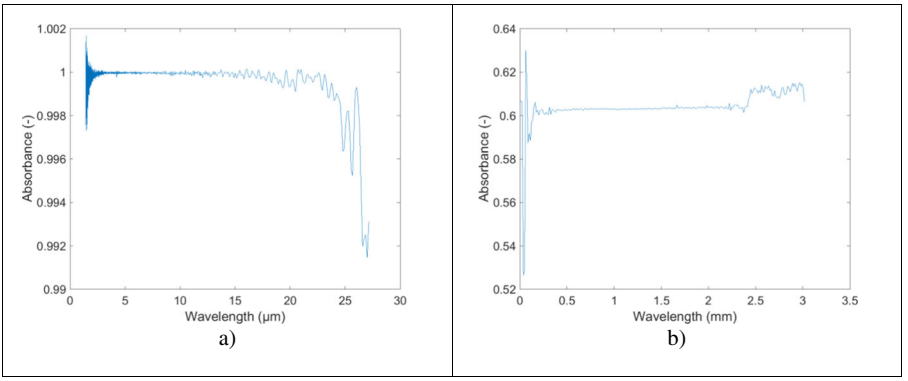

Fig. 3 Absorbance spectra of the photothermal converter: **a** from near- to far-IR (1 to 25 μm) and **b** in the millimeter range (0.1 to 3 mm)

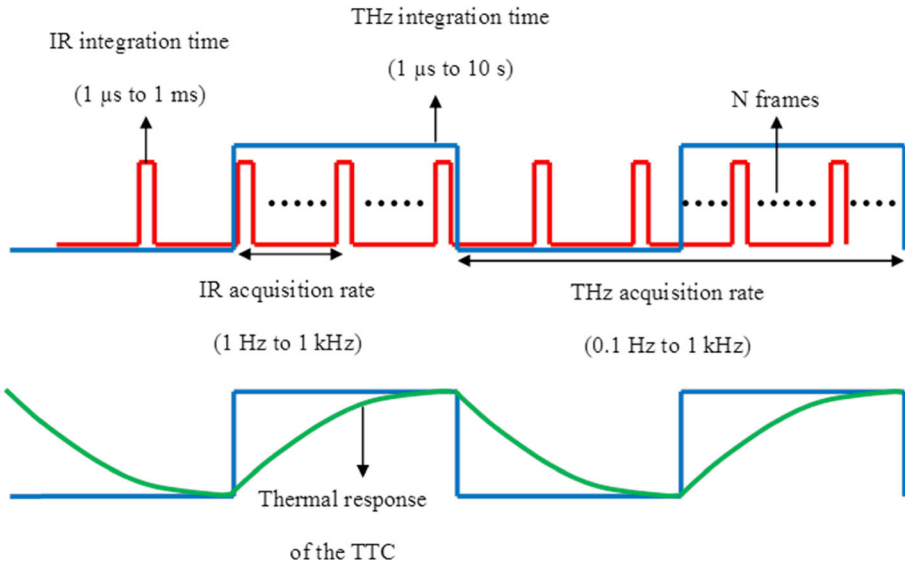

Fig. 4 Signal acquisition diagram: *top*, THZ integration time (THz-IT), IR integration time (IR-IT) and acquisition rate; *bottom*, TTC thermal response as a function of the THz acquisition rate

To reduce the noise, the spatial singular value decomposition (SVD) technique was applied to signals obtained after lock-in processing (see [19] for details):

$$A_{\mathrm{SVD}}(x,y) = \sum_{m=1}^{r_0} U_m(x) S_m V_m(y), \tag{2}$$

where $A_{\mathrm{SVD}}(x,y)$ is the signal amplitude after SVD decomposition, $U_m(x)$, $V_m(y)$ and S_m are the eigenvalues and eigenvectors of the decomposition, and r_0 is the mode number.

To illustrate the complete processing method, Fig. 5 shows a raw data image acquired within a period of 1 s at a frequency of 200 Hz. Figure 5a shows the normalized raw image at 0.5 s, Fig. 5b is obtained after implementing the four-image processing algorithm, and the image in Fig. 5c is obtained by applying the SVD technique. Finally, the beam profiles for each of the aforementioned images are presented in Fig. 5d.

3 Terahertz-to-Thermal Converter Efficiency

3.1 Thermal Conversion Modeling

As mentioned above, a photothermal sensor can be thermally described using a 2D transient model that contains a heat source determined by the sub-THz radiation characteristics and the convective and radiant heat losses. In the finite volume numerical formulation, the corresponding problem is given by:

where:

$$Fo_{i,j}\Delta T^k_{i,j} + \Phi^k_{i,j} - Bi_{i,j}\left(T^k_{i,j} - T_0\right) = \delta T^k_{i,j} \tag{3}$$

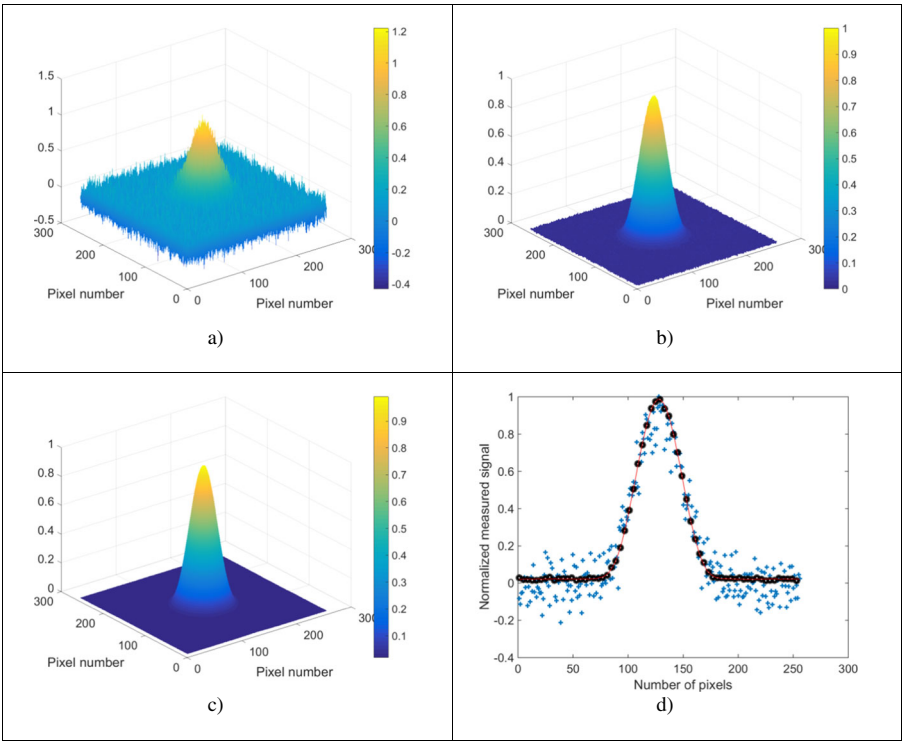

Fig. 5 Image processing results (1 s acquisition, 200 Hz frequency): **a** raw normalized data after 0.5 s, **b** after applying the four-image processing method Eq. (1), **c** after the SVD method Eq. (2) is applied to (**b**), and **d** the beam profiles across the image centers: **a** *crosses*, **b** *circles*, and **c** *line*

- $\Delta T_{i,j}^{k} = (T_{\mathrm{i}+1,\mathrm{j}}^{k} + T_{\mathrm{i}-1,\mathrm{j}}^{k} + T_{\mathrm{i},\mathrm{j}+1}^{k} + T_{\mathrm{i},\mathrm{j}-1}^{k} - 4T_{i,j}^{k})$ is the Laplacian
- $\delta T_{i,j}^{k} = T_{i,j}^{k+1} - T_{i,j}^{k}$ is the temperature derivative by time
- $\mathrm{Fo}_{i,j} = \frac{a_{i,j}\Delta t}{\Delta x^2}$ is the local Fourier number (dimensionless time); $a_{i,j}$ is the local thermal diffusivity ($\mathrm{m^2\ s^{-1}}$), $\Delta x = \Delta y$ is the pixel size (m), and Δt is the time step (s)
- $\mathrm{Bi}_{i,j} = \frac{2h_{i,j}\Delta t}{\rho C_p e}$ is the local Biot number; the parameter $h_{i,j} = \mathrm{hcv}_{i,j} + 4\varepsilon\sigma T_0^3$ specifies local heat losses due to convection $\mathrm{hcv}_{i,j}$ and linearized radiation $4\varepsilon\sigma T_0^3$ ($\mathrm{W\ m^{-2}\ K^{-1}}$), T_0 (K) is room temperature, ρC_p ($\mathrm{J\ m^{-3}\ K^{-1}}$) is the volumetric specific heat, e is the thickness of the photothermal converter (m), V is the volume ($\mathrm{m^3}$), $\Phi_{i,j}^{k} = \frac{Q_0 \Delta t}{\rho C_p V}$ is the equivalent heat source temperature in (K), and Q_0 (W) is the power of the incident THz radiation.

The model parameters used for the simulation are the following: thermal diffusivity, $a = 4 \times 10^{-7}$ $\mathrm{m^2\ s^{-1}}$; conductivity, $\lambda = 0.5$ $\mathrm{W\ m^{-1}\ K^{-1}}$; volume specific heat, $\rho C_p = 10^6$ $\mathrm{J\ m^{-3}\ K^{-1}}$; and total heat exchange coefficient, $h = 8$ $\mathrm{W\ m^{-2}\ K^{-1}}$, calculated by the correlation [22] and by the linearization of the radiant heat losses at room temperature. In the analysis, the sub-THz source is represented by a step function with $Q_0 = 1 \times 10^7$ W, a pixel size of $\Delta x = \Delta y = 250$ μm and an acquisition time step of $\Delta t = 200$ ms; the number of pixels in both the x and y directions is 256, and the number of time steps is 100. The results of thermal modeling are presented in Fig. 6. Specifically, Fig. 6a presents the heat source profile (μW),

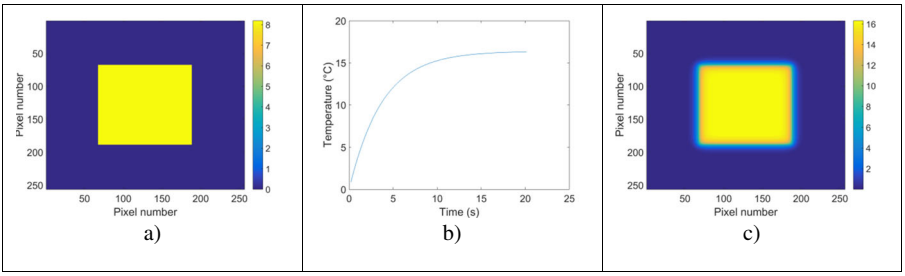

Fig. 6 Thermal modeling of the photothermal converter: **a** heat flux profile in microwatts, **b** temperature evolution as a function of time, and **c** steady-state temperature distribution

Fig. 6b shows the temperature response as a function of time, and Fig. 6c presents the steady-state distribution.

3.2 Calculating Conversion Rate

Because a photothermal converter can be considered to be a blackbody (see the IR absorption spectrum in Fig. 3a), the thermal flux conditioned by the converter temperature according to Eq. 3 and measured by the IR camera in 14-bit digital levels (DL) can be calculated using the following formula: $\Phi_{i,j}^{k} = \varepsilon\sigma S(T_{i,j}^{k4} - T_0^4)$. Thus, the conversion into temperature unit $T_{\circ C}$ can be performed using the DL to degree-Celsius calibration curve (supplied by the IR camera manufacturer): $T_{\circ C} = (-7.27 \times 10^{-12} T_{DL}^4 + 328.3 \times 10^{-9} T_{DL}^3 - 5.8 \times 10^{-3} T_{DL}^2 + 52.77\ T_{DL} - 164 \times 10^3)\mathrm{IT}(\mu s)$, where T_{DL} is the pixel-based signal in DL and IT is the integration time of the camera in the range from 1 to 2000 μs.

With the above assumptions, the pixel-based thermal conversion rate is given by the ratio between the thermal flux conditioned by the converter temperature and the incident heat flux:

$$\alpha_{i,j}^{k} = \frac{\varepsilon\sigma S\left(T_{i,j}^{k\,4} - T_0^4\right)}{Q_{0\,i,j}^{k}} \tag{4}$$

To illustrate the procedure described above, Fig. 7a shows the incident heat flux $Q_{0i,j}^{k}$ (μW), and the resulting radiant flux $\varepsilon\sigma S(T_{i,j}^{k\,4} - T_0^4)$ in microwatts is presented in Fig. 7b for the steady state. The maximum conversion rate as a function of time is shown in Fig. 7c for the central image pixel.

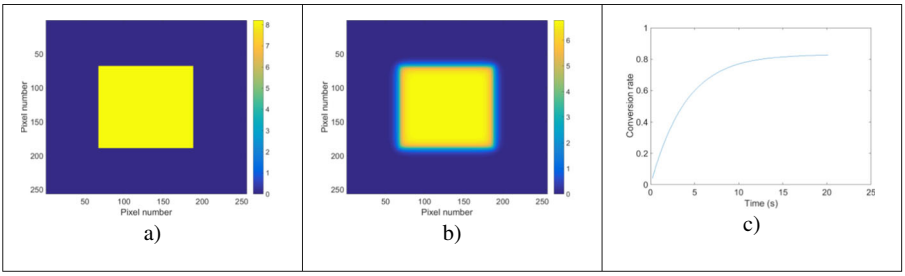

Fig. 7 Evaluation of the conversion rate: **a** incident square-shape heat flux (μW), **b** calculated steady-state heat flux in microwatts, and **c** maximum conversion rate as a function of time using Eq. (4)

Note that with the accepted thermal model parameters and the square-shape incident flux, the maximum conversion rate reached 0.8 at the steady state, while for short times (<1 s), the conversion was approximately 0.1 when the heat diffusion length did not exceed 1 pixel (see more details in Sect. 3.5).

3.3 Influence of the Beam Size

It is assumed that both the size of the radiation beam and its power affect the conversion rate. To illustrate this fact, the same beam power (20 μW per pixel) was applied in three incident beams: point-like (Fig. 8a), small square shape (Fig. 8b) and extended, or uniform, heat source (Fig. 8c). The corresponding thermal responses are shown in Fig. 8d–f along with the conversion rates.

Figure 8c shows that, in the case of a uniform heat source, the thermal response is that of a <<thermally thin wall>> (1D) subjected to heat losses, from which the in-plane heat diffusion may be negligible. Figure 8d shows the conversion rate resulting from the heat balance for each given light source as a function of time. This figure illustrates that the conversion rate tends to be the highest in the case of an extended uniform beam; the corresponding time to reach the steady state is 20 s (see Fig. 8e).

In contrast, the point-like source (Fig. 8a) behavior can be related to the 2D heat model due to significant in-plane diffusion. In this case, the time response is very fast, with the steady state achieved in 2 s and the conversion rate being only 0.02 (Fig. 8d, e, dot curve, "+"). Moreover, the square-shape (16 × 16 pixels) beam produces a conversion rate of approximately 1 (Fig. 8e, square "line"), and the steady state is reached after 20 s (Fig. 8d, square, "solid line"). The detailed analysis of the conversion rate as a function of the beam size is illustrated in Fig. 8f. As shown, a plateau is reached after 1 s if the beam size exceeds 4 pixels, accompanied by a low conversion value of 0.2. This figure demonstrates that the use of a *uniform or a Gaussian-shaped beam* provides a reasonable efficiency of the photothermal

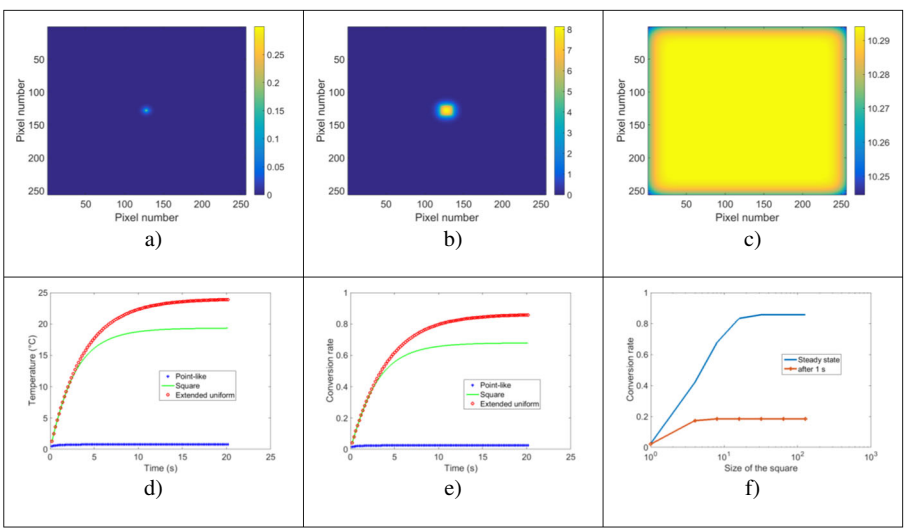

Fig. 8 Influence of the incident heat source geometry (steady-state case): **a** point-like source, **b** square source (16 × 16 pixels), **c** extended uniform heat source, **d** maximum thermal response for each case, **e** conversion rate as a function of time, and **f** semi-log(x) conversion rate as a function of source area size

conversion. To summarize, the above analysis shows that the conversion rate depends on the characteristic dimensions of the light source.

Similar observations regarding the beam size were previously reported. The results revealed that the beam size must be taken into account and that the Gaussian-like beam profile is recommended [8, 9].

3.4 Influence of the Incident Power

The radiation power influences the conversion rate in a non-linear manner, following Stefan-Boltzmann's law (the thermal flux is proportional to the fourth power of the temperature). This fact is illustrated in Fig. 9 (Gaussian source, steady-state case), where the relationship between the conversion rate (given by Eq. 4) and the thermal flux power is presented. In this consideration, the maximum power was limited to temperatures lower than 200 °C to avoid converter degradation; consequently, the maximum resulting temperature corresponded to a Gaussian-distributed power of approximately 1 W. Moreover, it has been found that the conversion rate is approximately 0.5 if the beam power value is 1–10 mW, and it increases as the power increases until the conversion rate reaches a value of approximately 4 at 1 W.

The influence of the incident power was also discussed by Zdanevicius et al. [11], who concluded that in the case of THz detectors, the situation is difficult because of unknown beam properties and inhomogeneous power distributions.

3.5 Influence of the Acquisition Time

In the steady state, the temperature distributions are blurred because of in-plane thermal diffusion in the bulk material [19]. Therefore, it is recommended to work at shorter times ($t < 1$ s) to avoid significant heat diffusion, thus ensuring that the temperature profile is close to the radiation beam profile. It has been found that at $t < 1$ s, the diffusion length is less than 1 pixel (pixel size is 250 μm in our case); thus, the temperature inversion procedure is not required to estimate the heat source characteristics. For example, Fig. 10 illustrates the effect of

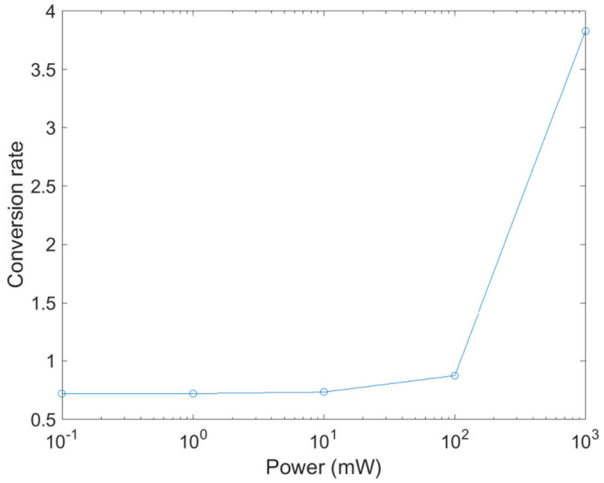

Fig. 9 Maximum conversion rate as a function of the incident source power (Gaussian source, steady state)

thermal diffusion in the case of a square (60 × 60 pixel) beam (chosen pixel 128 ± 30). The temperature profile along the x coordinate, which is presented in Fig. 10c for different times, shows that the image blurring involves approximately 15 pixels in the steady state and less than 1 pixel at 1 s (Fig. 10b). Hence, to appropriately reproduce the shape of the incident radiation, the converter with the specified parameters should operate at shorter times (less than 1 second in our case, Fig. 10a).

Note that because the infrared device is equipped with a photothermal converter, some temperature gradients are observed. This result is due to the in-plane thermal diffusion, and this phenomenon has a characteristic time on the order of seconds (time to reach the steady state); therefore, to have good accuracy, images should be acquired after this characteristic time. After the photothermal converter has reached the steady state, it is possible to work at the same acquisition frequency as the IR camera (200 Hz). Other imaging systems based on the use of FPA detectors reported image acquisition frequencies of 25 Hz when they used an antenna coupled with integrated CMOS [16] and 30–50 Hz systems using uncooled microbolometers [14, 15].

3.6 Calculating Camera Detectivity

For the IT time of 800 μs at room temperature, the minimum temperature variation corresponding to 1 DL signal of the IR camera is approximately 3 mK. In this case, the detectivity of a single pixel (size of 250 μm) was calculated as follows:

$$D = 5.67 \times 10^{-8}\left(\left(300 + 3 \times 10^{-3}\right)^4 - (300)^4\right) * \left(250 \times 10^{-6}\right)^2 \sqrt{800 \times 10^{-6}}$$

This detectivity level corresponds to the minimum heat flux that can be measured by the IR camera. By assuming that the conversion rate (see part 3 because conversion depends on the shape and size of the source beam) efficiency of the photothermal converter can vary in a range of 0.2 to 1 at $t = 1$ s (Fig. 8e, Gaussian source, steady state), we obtain the detectivity of the photothermal converter given by the measurements of the infrared camera at a level of 160 pW $Hz^{-0.5}$ per pixel when only 0.2 of the total flux is converted.

Let us compare the detector's sensitivity employing bolometric or other thermoelectric detection approaches, which are often based on well-developed infrared imager technologies adjusted to THz frequencies. In this case, the INO's THz detectors for the IRXCAM-160 and IRXCAM-384 cameras at 70.4 μm (4.25 THz) NEP values were reported to be 79 and 24.7 pW $Hz^{-0.5}$, respectively [15]. The performance of the IRXCAM-160 was found to be on the same order of magnitude as the one reported by various groups worldwide using

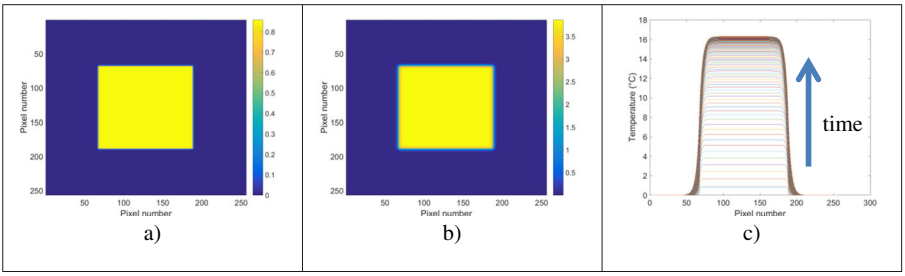

Fig. 10 Thermal diffusion over time: **a** temperature distribution at $t = 0.2$ s, immediately after energy discharge, **b** temperature distribution at $t = 1$ s, and **c** temperature profiles along the x direction at different times

different technologies for THz imaging summarized by Oda et al. [14] of NEC in 2015. The performance of IRXCAM-384 and NEC is comparable. In addition, NEP values that can vary from 26 pW $Hz^{-0.5}$ [16] to 260 pW $Hz^{-0.5}$ [11] have been reported for FPAs based on antenna-coupled FETs for THz detection (TeraFETs), which have been implemented in standard CMOS technology. The difference in the average NEP value can be explained by differences in pixel size, detector bandwidth and pixel responsivity.

4 Sub-THz Imaging Acquisition Results

4.1 Sub-THz Beam Characterization

By using the setup and measurement technique described above, the first experiments were performed to determine the profile of the Gunn diode radiation (200 Hz frequency). The THz-IT and IR-IT values were set to 1 s and 800 μs, respectively. The data processing was performed by applying the 4-image algorithm and the SVD technique according to Eqs. (1) and (2). The results are presented in Fig. 11, including the raw image (Fig. 11a), the image processed by applying the four-image algorithm (Fig. 11b), the image after applying SVD at $r_0 = 3$ (Fig. 11c) and, finally, the thermal x coordinate responses across the image centers (Fig. 11d).

The obtained experimental results demonstrate that the use of the SVD technique in sub-THz imaging by combining TTC and an IR imager allows for a reduction in the acquisition time and an improvement in the image quality. For example, depending on the beam power, the SVD technique allows for obtaining a sharp sub-THz image within 1 ms compared with the image acquisition time of 1 s.

Furthermore, depending on the material optical transparency in the sub-THz band, the experimental parameters, such as THz-IT, acquisition frequency and the number of eigenvalues (r_0), should be carefully chosen to obtain THz images of good quality.

4.2 One-Shot THz Imaging of a Metallic Object Inside a Cardboard Box

Figure 12 shows the THz image of a metallic object inside a cardboard box. The image diameter was 5 cm (size of the incident beam and TTC), the THz-IT was 100 ms, and the SVD approach was applied at $r_0 = 3$.

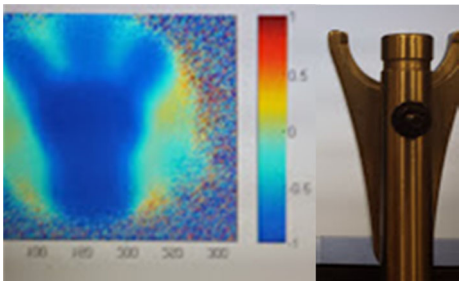

Fig. 11 Experimental measurements for a Gunn diode square illumination of 1 s and an IR camera acquisition of 1 s at a frame rate of 200 Hz: **a** raw normalized data after 0.5 s; **b** amplitude after demodulation using the four-image method (1); **c** same as (**b**), after application of the SVD method using the results of (**b**) in Eq. (2); and **d** comparison of the profiles at the center of images: **a** *empty circles*, **b** *solid line*, and **c** *crosses*

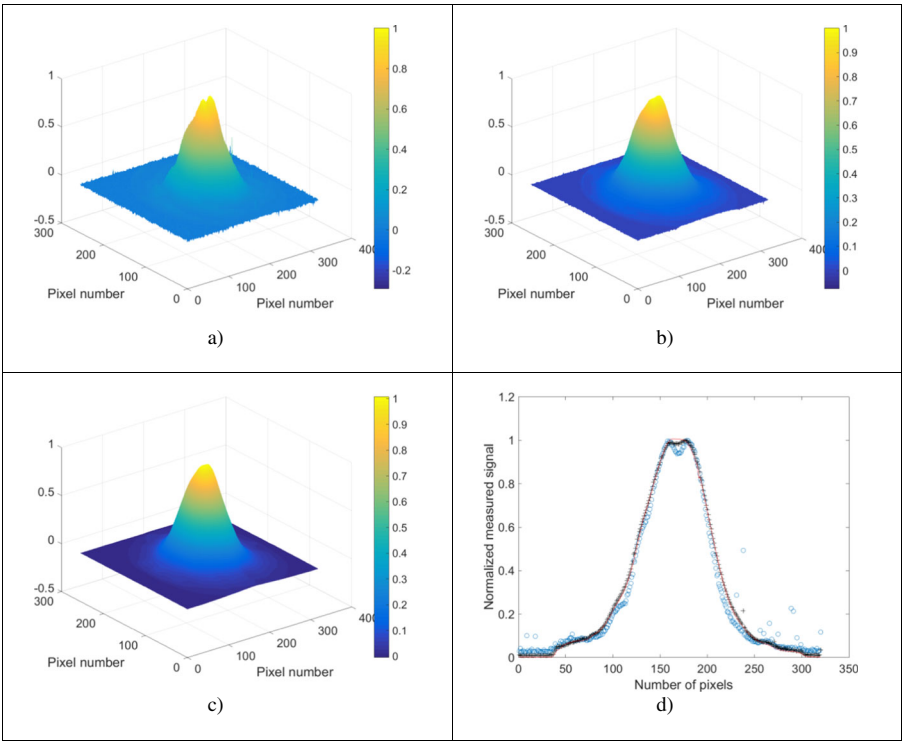

Fig. 12 THz imaging of a metallic object inside a cardboard box (*left*, the resulting THz image; *right*, photograph of the object outside of the cardboard box)

Fig. 13 THz image of an A4 paper sheet with metallic letters writing the phrase <<HELLO TREFLE>> placed inside a postcard envelope (scanning technique, 6 × 7 shots taken for approximately 2 min)

4.3 Scanning THz Imaging of an A4 Paper Sheet Through an Envelope

A sheet of A4 size paper (21 × 29.7 cm) containing letters made from metallic foil was placed in an envelope. The THz image shown in Fig. 13 was obtained in 2 min using a scanning technique (6 × 7 shots) to achieve a reasonable image quality.

5 Conclusions

A novel method has been presented for sub-THz imaging, particularly for non-destructive purposes. The imaging system consists of a modulated continuous wave sub-THz source, a photothermal converter that performs spectral conversion (from the millimeter range to near- and mid-infrared ranges) and a standard quantum IR thermographic camera. The thermographic signal is demodulated (lock-in technique) and improved by applying SVD processing.

The signal-to-noise ratio strongly depends on the source power, the thermal conversion ratio of the TTC and the IR camera sensitivity. Regardless of these parameters, the use of SVD significantly increases the thermal conversion ratio and drastically decreases the acquisition time.

Depending on the required spatial resolution of the sub-THz image, the integration time of the sub-THz imager (the THz illumination duration) has been accordingly adjusted. This time depends on the thickness and thermal diffusivity of the photothermal converter being independent of the processing method. In the present case, this time should not exceed 1 s to avoid image blurring.

Some simple experimental demonstrations of using sub-THz imaging in non-destructive evaluations (NDE) have demonstrated a detectivity of approximately 160 pW $Hz^{-0.5}$ per pixel if only 20 % of the heat flux is being converted. This value should be further improved to match commercial imaging systems, which report NEP values of up to 20–70 pW $Hz^{-0.5}$. To enhance sensitivity, a more complicated NDE configuration is foreseen, in particular, by using sub-THz tomography. Such a technique, combined with signal processing methods, appears to be interesting for real-time NDE applications. The advantage of the described technique is the possibility of using a standard IR camera, thereby reducing the investment cost for only a thermal converter. The work reported was limited to the sub-THz domain, not because the imager was intrinsically limited to this domain but because we do not have a higher frequency source with enough power. The photothermal converter has a very large bandpass for electromagnetic waves and can be used in the full THz domain.

References

1. Ouchi, T., Kajiki, K., Koizumi, T., Itsuji, T., Koyama, Y., Sekiguchi, R. & Kawase, K, Terahertz imaging system for medical applications and related high efficiency terahertz devices, **J Infrared Millim Terahertz Waves**, *35*(1), 118–130 (2014)
2. Tomaino, J. L., Jameson, A. D., Kevek, J. W., Paul, M. J., van der Zande, A. M., Barton, R. A. & Lee, Y. S, Terahertz imaging and spectroscopy of large-area single-layer graphene**. Opt Express,** *19*(1), 141–146 (2011)
3. Chan, W. L., Deibel, J.& Mittleman, D. M, Imaging with terahertz radiation**. Rep Prog Phys**, 70(8), 1325 (2007)
4. Jansen, C., Wietzke, S., Peters, O., Scheller, M., Vieweg, N., Salhi, M & Koch, M., Terahertz imaging: applications and perspectives. **Appl Optics**, *49*(19), E48-E57 (2010)

5. Hu, B. B., Nuss, M. C. & Hu, B. B, Imaging with terahertz waves, **Opt Lett**. 20(16), 1716–1718 (1995)
6. Jepsen, P. U., Cooke, D. G. & Koch, M, Terahertz spectroscopy and imaging—modern techniques and applications, **Laser Photonics. Rev** 5(1), 124–166 (2011)
7. Mittleman, D. M., Gupta, M., Neelamani, R., Baraniuk, R. G., Rudd, J. V. & Koch, M, Recent advances in terahertz imaging. **Applied Physics B**, 68(6), 1085–1094 (1999)
8. Müller, R., Bohmeyer, W., Kehrt, M., Lange, K., Monte, C. & Steiger, A. Novel detectors for traceable THz power measurements. **J Infrared Millim Terahertz Waves**, 35(8), 659–670 (2014)
9. Wegner L., Hübers H. W., Meindl P., Richter H. & Steiger A., Towards traceable radiometry in the terahertz region, **Metrologia,** 46, S160 (2009).
10. Oda, N., Hosako, I., Ishi, T., Minamide, H., Otani, C. & Sekine, N. The need of terahertz cameras for standardizing sensitivity measurements, **J Infrared Millim Terahertz Waves**,35(8), 671-685(2014).
11. Zdanevičius, J., Bauer, M., Boppel, S., Palenskis, V., Lisauskas, A., Krozer, V. & Roskos, H. G, Camera for High-Speed THz Imaging, **J Infrared Millim Terahertz Waves**,1-12 (2015).
12. Narlis, E. O. Comparative performance analysis of the MWIR and LWIR focal plane array starring imaging infrared systems. **J Infrared Millim Terahertz Waves**, *23*(3), 393-408(2002).
13. Pope, T., Doucet, M., Dupont, F., Marchese, L., Tremblay, B., Baldenberger, G. & Lamontagne, F, Uncooled detector, optics, and camera development for THz imaging. **In Proc. SPIE** 7311-73110L (2009)
14. Oda, N., Kurashina, S., Miyoshi, M., Doi, K., Ishi, T., Sudou, T. & Sasaki, T, Microbolometer terahertz focal plane array and camera with improved sensitivity in the sub-terahertz region. **J Infrared Millim Terahertz Waves**, 36(10), 947–960 (2015).
15. Dufour, D., Marchese, L., Terroux, M., Oulachgar, H., Généreux, F., Doucet, M. & Bergeron, A. Review of terahertz technology development at INO. **J Infrared Millim Terahertz Waves**, 36(10), 922–946 (2015).
16. Oden, J., Meilhan, J., Lalanne-Dera, J., Roux, J. F., Garet, F., Coutaz, J. L. & Simoens, F, Imaging of broadband terahertz beams using an array of antenna-coupled microbolometers operating at room temperature. **Opt Express**, 21(4), 4817–4825 (2013).
17. Meilhan, J., Simoens, F., Lalanne-Dera, J., Gidon, S., Lasfargues, G., Pocas, S. & Ouvrier-Buffet, J. L, Terahertz frequency agility of uncooled antenna-coupled microbolometer arrays. 37th International Conference of Infrared, Millimeter, and Terahertz Waves, Thu-B-1-2 (2012).
18. Pradere, C., Caumes, J. P, Toutain, J, Abraham, E, Chassagne, B & Batsale, J.C, Absolute self-calibrated room-temperature terahertz powermeter, **Appl Optics**, 52(11), 2320–2324, (2013)
19. Pradere, C., Caumes, J.P., Balageas, D, Salort, S, Abraham, E., Chassagne, B. & Batsale, J.C. Photothermal converters for quantitative 2D and 3D real-time terahertz imaging, **Quant Infrared Thermogr J**, 7(2), 217-235(2010).
20. Pradere, C., Caumes, J. P, Chassagne, B & Batsale, J.C, Patent FR0952097 (2009)
21. Rampnoux, J. M., Michel, H., Salhi, M. A., Grauby, S., Claeys, W., & Dilhaire, S. Time gating imaging through thick silicon substrate: a new step towards backside characterisation. **Microelectron Reliab**, 46(9), 1520–1524. (2006).
22. Bird, R. B. Transport phenomena. **Appl Mech Rev,** *55*(1) (2002)